Noninvasive Glucose Sensor Based on Parity-Time Symmetry

Yun Jing Zhang, Hoyeong Kwon, Mohammad-Ali Miri, Efthymios Kallos, Helena Cano-Garcia, Mei Song Tong, and Andrea Alu

Phys. Rev. Applied **11**, 044049 — Published 16 April 2019

DOI: 10.1103/PhysRevApplied.11.044049

A Non-Invasive Glucose Sensor Based on Parity-Time Symmetry

Yun Jing Zhang,[1,2] Hoyeong Kwon,[1] Mohammad-Ali Miri,[1,3,4] Efthymios Kallos,[5] Helena Cano-Garcia,[5,6] Mei Song Tong,[2,†] and Andrea Alu,[1,4,7,8*]

[1]Department of Electrical and Computer Engineering, The University of Texas at Austin, Austin, 78712, USA

[2]Department of Electronic Science and Technology, Tongji University, Shanghai, 201804, China

[3]Department of Physics, Queens College of the City University of New York, Queens, New York 11367, USA

[4]Physics Program, Graduate Center, City University of New York, New York 10016, USA

[5]Medical Wireless Sensing Ltd, London, E1 2AX, UK

[6]King's College London, London, WC2R 2LS, UK

[7]Photonics Initiative, Advanced Science Research Center, City University of New York, New York 10031, USA

[8]Department of Electrical Engineering, City College of The City University of New York, New York 10031, USA

We discuss a non-invasive technique to detect glucose changes with enhanced sensitivity based on parity-time (PT) symmetry. We detect glucose level changes within the skin by measuring the frequency shift in the electromagnetic resonance induced within a PT-symmetric system that sandwiches the tissue sample under analysis. Even though the sample itself is lossy, and therefore resonances would be damped, the introduction of balanced gain and loss enables an efficient sensing mechanism that bypasses the conventional limitations of passive sensing schemes. Our results indicate that the resonance shift can be made fairly linear with respect to the glucose concentration variations, and the expected accuracy is large. We also investigate a realistic system to implement the non-invasive PT-symmetric glucose

*aalu@gc.cuny.edu

† mstong@tongji.edu.cn

sensor using loop antennas and negative impedance converters, exploring its sensitivity with respect to design errors and disorder.

I. INTRODUCTION

Non-invasive measurements of physiological properties of human or animals are of great importance, because they can avoid irritation and infection of tissues and organs. In particular, non-invasive detection of glucose concentration has been investigated for many years [1,2]. In general, there are several types of non-invasive glucose sensors-based on electromagnetic radiation, with common glucose sensors utilizing optical frequencies [3,4]. These short wavelengths, however, imply larger errors from non-conformal skin, interstitial fluid concentration, etc. In addition, the equipment required for optical sensing is typically expensive and bulky. Combined with optical sensors, metabolic heat conformation has been explored [5], resulting in enhanced accuracy at the expense of additional complexity and cost, due to the required multi-signal sensing, while, portability imposes additional restrictions. Electrochemical glucose sensors have been also proposed, which indirectly measure two analytes, interstitial fluid (ISF) and sweat [6-9], using the relationship between these analytes and glucose concentration, resulting in an improved sensitivity. However, such methods require attaching electrodes to the skin, which is not desirable. In addition, the time lag between changes in the blood, ISF glucose concentrations and sweat contamination can result into errors.

Electromagnetics-based glucose detection, on the other hand, is inherently low cost, and less complex compared to other approaches. For example, impedance spectroscopy was used in the frequency range of 40 MHz – 1600 MHz with high precision. Yet, the technique suffers from certain problems, including influences from the thickness and moisture of skin, which introduce large losses and the necessity of clamp relocation. Based on the reflection and transmission characteristics of glucose, a waveguide model (up to 40 GHz) was shown to detect glucose changes with 0.1wt% precision, but with fair error [10]. Microwave cavity resonator setups have also been used [11], but are impractical to use with realistic samples. Applied to skin-capillary-skin structures (like the earlobe or finger-web), millimeter-waves techniques have been used in [12,13], enabling the detection of glucose weight percent as small as 0.024wt%. However, utilizing the slight variation of reflection and transmission amplitude requires a high-precision measuring equipment, for instance, a

vector network analyzer (VNA).

Along different lines, recently there has been a growing interest in investigating electromagnetic configurations that involve gain and loss, with special relevance for sensing purposes. Interest in such systems has been originally triggered by developments in quantum mechanics, showing that certain class of non-Hermitian Hamiltonians can exhibit entirely real energy spectra [14]. Such peculiar Hamiltonians commute with the parity-time (PT) operator, and are thus called PT-symmetric. In this regard, the similarities of the underlying mathematical formalism have allowed for exploring these notions in the context of electromagnetism [15]. In electromagnetics, PT-symmetric structures involve balanced regions of gain and loss [16]. Although loss has been long considered a foe for signal transport, the notion of PT-symmetry has changed the common views in that loss has become a new degree of freedom for designing electromagnetic structures with desired properties. Interestingly, it has been shown that PT-symmetric structures exhibit several novel features, including power oscillations [17], loss-induced transparency [18], unidirectional invisibility [19] and negative refraction [20]. These features enlighten some promising applications in several fields including optical absorbers [21], single-mode-selective PT-micro-ring lasers [22,23], invisible acoustic sensors [24], PT-symmetry teleportation [25], PT-symmetric wireless power [26]. An interesting feature of PT-symmetric structures is the emergence of an Anisotropic Transmission Resonance (ATR) for one-dimensional structures, at which, while the transmission is unity in both directions, the reflection coefficients becomes zero only in one direction [27,28]. Given that the ATR is related to the ratio of the gain-loss parameter to the coupling between the gain and loss layers, it offers an ultra-high sensitivity to the parameters involved, including the distance between loss and gain elements [29]. This interesting property creates a promising route to realize a hypersensitive sensor to detect micro-changes of analytes, which can be utilized to design a superior non-invasive glucose sensor. Noteworthily, even though here, we focus on non-invasive sensing of glucose, similar methods can be applied to other physiological properties of human or animals.

In this work, we propose a non-invasive method to detect glucose changes based on the concept of PT-symmetry. We focus on the earlobe or finger-web as the detecting location, given that these regions can be modeled as skin-capillary-skin and provide a

precise change in glucose concentration [30]. The condition of PT symmetry can be realized in the skin-capillary-skin system in order to create an anisotropic transmission resonance (ATR). The sensing mechanism is based on evaluating the frequency shift in this resonance versus the concentrations of glucose. In fact, the frequency shift of ATR is correlated with micro-variations of permittivity of glucose blood, thus the concentration of glucose can be tracked accurately through this feature [31-33]. We analyze this system through transmission-line theory, realizing the conditions of PT-symmetry with a non-Foster circuit [34].

In this work, we consider an RF circuit design at f_0~4 GHz. The weight percentage of glucose, wt%, in the proposed device can be written in terms of the frequency shift, Δf, as follows

$$\text{wt\%} = \alpha \frac{\Delta f}{f_0} \times 100\% \tag{1}$$

where, α is a proportionality constant, which is found to be 400. According to this relation, compared to current non-invasive glucose sensors, in this approach the lower bound on glucose detection resolution is determined by the frequency resolution of the RF components. Hence, using off-the-shelf RF transmitters and receivers with a frequency resolution of 100 kHz, a precision of 0.01wt% can be obtained. In addition, compared to other approaches based on the amplitude of transmission or reflection, the resonant-frequency-shift-based detection provides a better accuracy, while it can be easily calibrated.

This work is organized as follows. We first introduce our geometry, consisting of a multilayer structure of skin and capillary, and described through a transmission-line model in Section II. Section III investigates realistic skin-capillary-skin structures by including the loss in each layer, and it proposes a basic configuration for PT-symmetric glucose sensor. Introducing loaded loop antennas, Section IV introduces a practical 3D glucose sensor and explores its sensitivity to key devices and sample parameters. Finally, we consider a realistic NIC load with dispersive impedance in Section V, predicting good performance for the proposed sensor within a realistic antenna implementation.

II. PT-SYMMETRIC SENSOR AND ITS TRANSMISSION LINE MODEL

The geometry considered throughout this paper to realize a non-invasive glucose sensor consists of a 1-D parity-time symmetric multilayered system, which may be

schematically modeled with the simplified transmission line model in Fig. 1. Here, Z_p and Z_0 are the characteristic impedance of the ports and of the transmission line segments. The load impedance Z at the input port is set to a real value, representing a lossy resistance, while to maintain a balanced gain and loss in the structure we assume an active shunt load, represented by the negative resistance $-Z$, at the output port.

The scattering matrix of this simplified system is given by [35]

$$S = \begin{pmatrix} r_L & t \\ t & r_R \end{pmatrix} = \begin{pmatrix} \frac{j\left(-\frac{2}{\gamma}+\frac{1}{\eta}-\eta+\frac{\eta}{\gamma^2}\right)\sin k_l d}{2\cos k_l d + j\left(\eta+\frac{1}{\eta}-\frac{\eta}{\gamma^2}\right)\sin k_l d} & \frac{2}{2\cos k_l d + j\left(\eta+\frac{1}{\eta}-\frac{\eta}{\gamma^2}\right)\sin k_l d} \\ \frac{2}{2\cos k_l d + j\left(\eta+\frac{1}{\eta}-\frac{\eta}{\gamma^2}\right)\sin k_l d} & \frac{j\left(\frac{2}{\gamma}+\frac{1}{\eta}-\eta+\frac{\eta}{\gamma^2}\right)\sin k_l d}{2\cos k_l d + j\left(\eta+\frac{1}{\eta}-\frac{\eta}{\gamma^2}\right)\sin k_l d} \end{pmatrix} \tag{2}$$

where r_L, r_R are the reflection coefficients from left and right, t is the transmission coefficient, which is the same from both ports because of reciprocity. The parameter γ represents the ratio of the load impedance Z to the characteristic impedance of the transmission line Z_0. η is the ratio of the characteristic impedance of the ports Z_p to Z_0, ω is the angular frequency and k_l is the transmission-line wave number. Finally, μ is the permeability of free-space, given that the considered materials are non-magnetic.

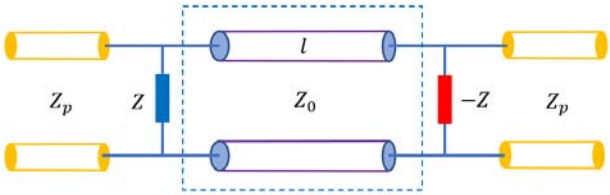

FIG. 1. PT-symmetric transmission line model

It is straightforward to verify that the model in Fig. 1 satisfies the parity-time symmetry relation $r_L r_R = t^2(1 - 1/|t|^2)$ [27]. When

$$\frac{1}{\gamma} = \frac{1}{\eta} \pm 1 \tag{3}$$

substituting Eq. (3) into (2) reduces to

$$S = e^{\pm j k_l d}\begin{pmatrix} 0 & 1 \\ 1 & j2\left(\frac{1}{\eta} \pm 1\right)\sin k_l d \end{pmatrix}, \tag{4}$$

which corresponds to an ATR, i.e., $|t| = 1$, and one of r_L or r_R vanishes. It is worth mentioning that ATRs can be obtained only when Eq. (3) is satisfied.

From Eq. (2), the eigenvalues of the scattering matrix can be found as

$$s_{\pm} = \frac{j\left(\frac{1}{\eta}-\eta+\frac{\eta}{\gamma^2}\right)\sin k_l d \pm 2\sqrt{1-\frac{1}{\gamma^2}\sin^2 k_l d}}{2\cos k_l d + j\left(\eta+\frac{1}{\eta}-\frac{\eta}{\gamma^2}\right)\sin k_l d} \tag{5}$$

It is noted that exceptional points occur when $k_l d = \arcsin\gamma$, which depend on the length of the transmission line. In addition, we can see that the exceptional points are not necessarily coincident with the ATR points.

If Z_p and Z are given, Eq. (3) leads to the ATR condition ($|t| = 1$)

$$Z_0 = \pm\frac{ZZ_p}{Z_p - Z} = \xi, \tag{6}$$

indicating an ATR can be achieved by adjusting either the load impedance Z or port characteristic impedance Z_p for arbitrary length of the transmission line.

The transmission line with effective permittivity $\epsilon_e = \epsilon(\omega, l)$ can represent any material inset between two ports, where l is the length of the transmission line. Given that $Z_0 = \omega\mu/k_l$ and $k_l = \omega\sqrt{\mu\epsilon_e}$, Eq. (6) reduces to

$$\sqrt{\frac{\mu}{\epsilon(\omega,l)}} = \xi, \tag{7}$$

where passivity requires $Re(\xi) > 0$. Equation (7) shows that the ATRs relate the angular frequency to the length of the transmission line. However, it is noted that the explicit analytical relation depends on the specific transmission line configuration.

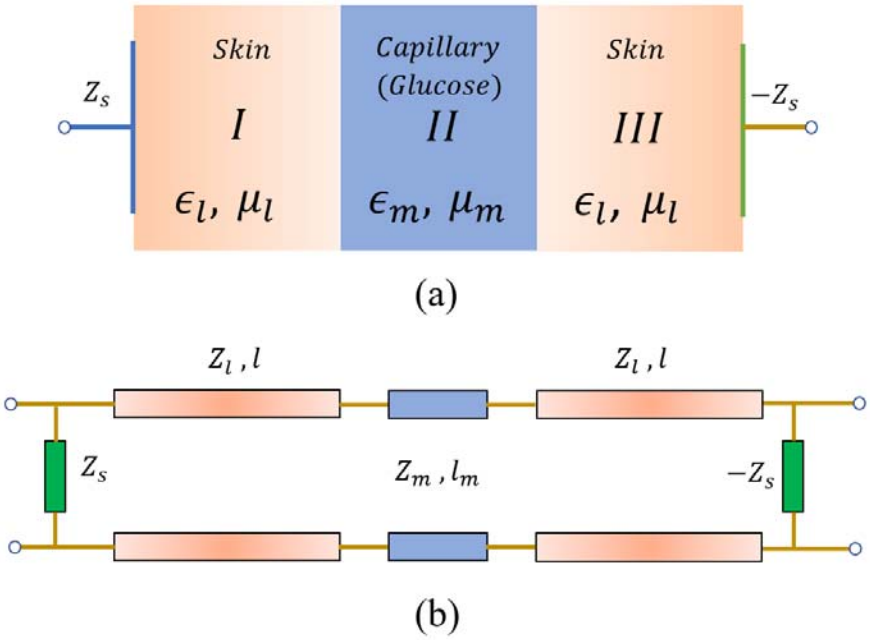

FIG. 2. (a) Geometry of the proposed PT-symmetric sensor composed of skin (I, III) and capillary (II) layers. Here, Z_s shows the load impedance while $-Z_s$ shows a supporting impedance that creates the condition of PT-symmetry. The material parameters ϵ, μ represent the permittivity and permeability of the different layers. (b) Transmission-line model of the sensor. The characteristic impedance of the skin and capillary layers is represented with Z_l

and Z_m respectively, while l_m and l indicate the corresponding lengths.

Based on this simple transmission-line model, we now consider the model of the sample under analysis as a multilayered electromagnetic structure (Figure 2(a)), composed by two skin layers sandwiching a glucose layer. Following the transmission line model in Fig. 1, this system is loaded on the front side by a passive impedance layer Z_s, while the other end is terminated with the negative conjugate impedance $-Z_s$. As above, this system is expected to support ATR resonances [25,36-37] under analogous conditions as derived above. In the following, we exploit the inherent sensitivity of PT-symmetric shunt impedances to the channel in between to monitor small glucose changes in the multilayer. As shown in Fig. 2(b), this structure can be readily modeled with a slightly more complex transmission-line model, which captures the central glucose region, but does not drastically change the physical mechanism for sensing compared to Fig. 1. In order to simplify the model and provide insights to the sensing mechanism, in this section we make two idealizations: first, we assume the transmission lines to be lossless, while in reality these layers involve intrinsic losses due to absorption. Furthermore, we neglect the effect of dispersion, although material dispersion plays a role in these layers. As we discuss later, these idealizations can be uplifted in a more realistic design of the sensor, and the sensing mechanism still works well after considering material loss and dispersion.

Comparing the model in Fig. 1 with the one in Fig. 2b, the characteristic impedance Z_0 in the previous analysis should be replaced by the effective characteristic impedance Z_e, where Z_e is defined by Z_l, Z_m, l and l_m. The value of Z_e can be accurately determined using the transfer matrix method.

The transfer matrices of the three transmission-line sections can be written as

$$T_{s\pm} = \begin{pmatrix} 1 & 0 \\ \pm 1/Z_s & 1 \end{pmatrix} \tag{8}$$

$$T_l = \begin{pmatrix} \cos(\beta l) & jZ_l \sin(\beta l) \\ j\frac{1}{Z_l}\sin(\beta l) & \cos(\beta l) \end{pmatrix} \tag{9}$$

$$T_m = \begin{pmatrix} \cos(\beta_m l_m) & jZ_m \sin(\beta_m l_m) \\ j\frac{1}{Z_m}\sin(\beta_m l_m) & \cos(\beta_m l_m) \end{pmatrix} \tag{10}$$

where, β and β_m represent the propagation constants for the skin and glucose layers

respectively. The total transfer matrix of the circuit is then given by

$$T_t = T_{s+}T_lT_mT_lT_{s-} = \begin{pmatrix} a & b \\ c & d \end{pmatrix}. \tag{11}$$

Finally, we calculate the reflection and transmission coefficients [38]

$$\begin{pmatrix} a & b \\ c & d \end{pmatrix} \Rightarrow \begin{pmatrix} r_L & t \\ t & r_R \end{pmatrix}. \tag{12}$$

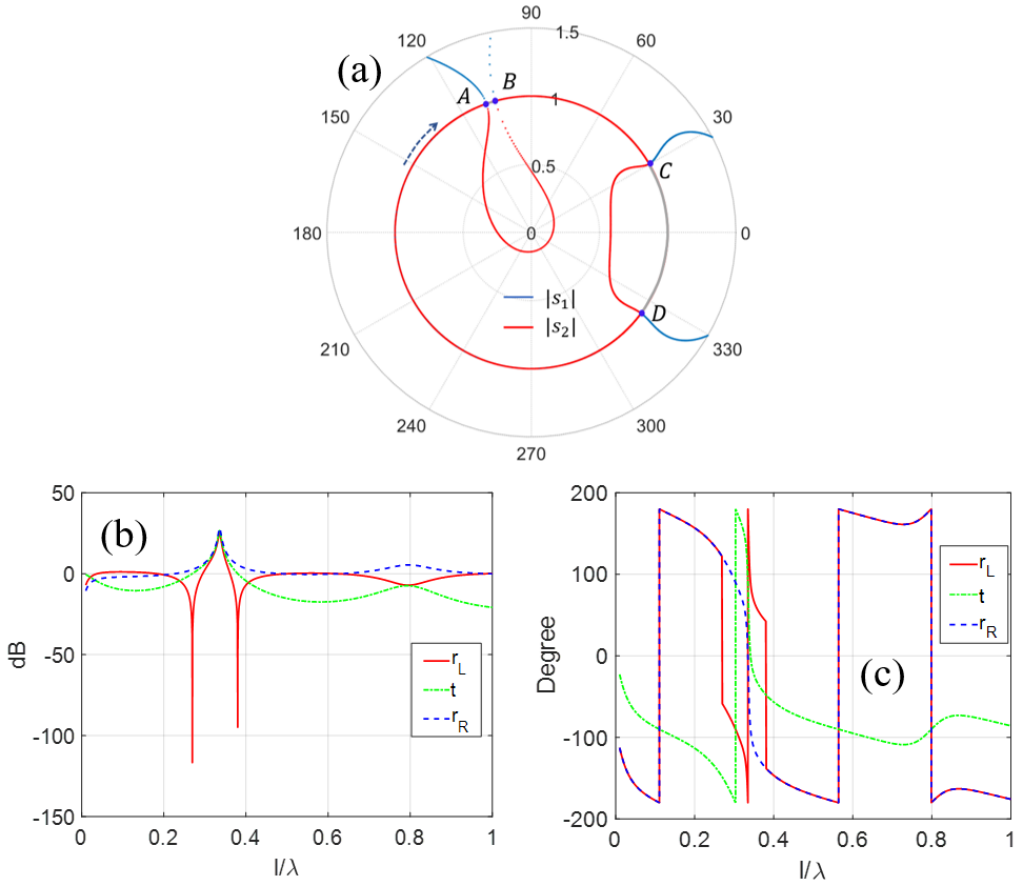

FIG. 3. Eigenvalues (s_1, s_2) of the scattering matrix in the unitary circle (a), magnitude (b) and phase (c) of the scattering coefficients of the PT-symmetric system in Fig. 2 versus normalized frequency (l/λ). Here, we have assumed $Z_l/Z_0 = 0.1326$, $Z_m/Z_0 = 0.0265$, $Z_s/Z_0 = 0.2122$, and $l_m/l = 0.1$. Two ATRs are observed at 0.27 and 0.38 l/λ, with out-of-phase and in-phase response, respectively.

Figure 3(a) shows the eigenvalues of the scattering matrix in the complex plane versus l/λ, which satisfy the condition $|s_1||s_2| = 1$ [27]. This figure shows two regions (A~B and C~D), with broken PT-symmetry phases ($0.327 < l/\lambda < 0.362, 0.704 < l/\lambda < 0.902$). Outside of these regions, the eigenvalues are unimodular, i.e., $|s_1| = |s_2| = 1$, and they are located on the unitary circle. At the phase transition

point, the two eigenvalues, and their associated eigenvectors, coalesce at an exceptional point singularity.

Figures 3(b, c) show the scattering coefficients and phase of the PT-symmetric transmission line system shown in Fig. 2(b) versus the ratio of the length of the side transmission-line segments to the wavelength. Figure 3(b) clearly shows two ATRs occurring at critical lengths l/λ =0.38 and 0.27, which are in the unbroken-phase region. Eq. (6) is satisfied at these two points, and the phase of the scattering coefficients, shown in Fig. 3(b), shows a π phase jump in the left reflection at the resonance frequencies.

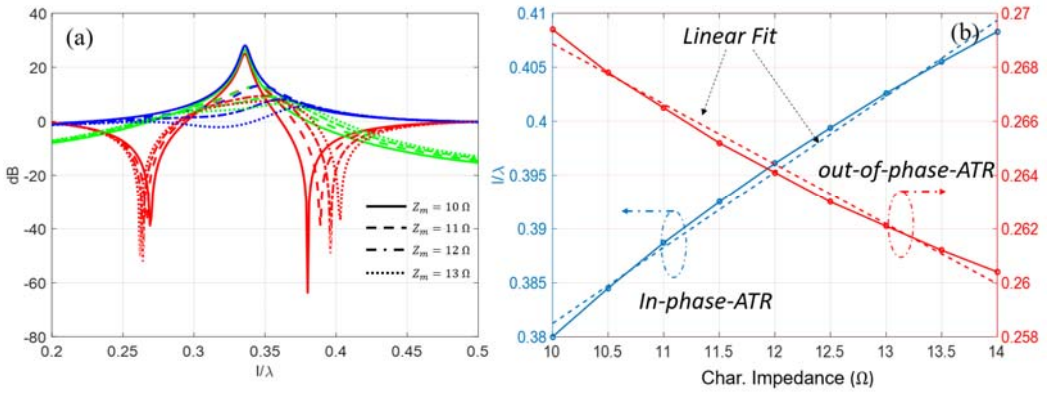

FIG. 4. (a) Scattering coefficients versus normalized frequency for different values of the characteristic impedance of the center transmission line (the glucose layer). (b) ATR frequencies with respect to the characteristic impedance of the center transmission line. The dashed lines represent linear trends fitted to the ATR curves.

Here we are interested in exploring the dynamics of these sharp ATRs with respect to the characteristic impedance of the center transmission line, i.e., the relation between Z_m and Z_e. Figure 4(a) shows the scattering parameters of the overall system versus normalized frequency for different values of the characteristic impedance of the center line Z_m. The change in ATRs with respect to this impedance is plotted in Fig. 4(b). According to this figure, the trends are fairly linear in the depicted range of Z_m, which is ideal for sensing purposes. In addition, as shown in Fig. 4(b), for a certain range the in-phase ATR has more sensitivity to the impedance compared to the out-of-phase ATR. Hence, by detecting the shift of the in-phase ATR, a small variation of characteristic impedance or length of the middle section can be detected with large sensitivity. These results show that the PT-symmetric pair

operating around the ATR resonances forms an ideal basis for a non-invasive sensor. Next, we apply this geometry to a practical glucose sensing problem.

III. SKIN-GLUCOSE-SKIN MULTILAYER

We now focus on the realistic problem of the skin-glucose-skin (SGS) multilayer of Fig. 2(a). As discussed in Ref. [39], the skin permittivity can be described with a Cole-Cole dispersion model. The capillary substance can approximate the glucose/water solution with high accuracy [40,41], which obeys a Debye model with linear relation with the glucose concentration [42-44]. Here, we assume that the incident wave in the SGS model is a plane wave, and the multilayer is infinite in the transverse dimensions, such that the transmission-line model of Fig. 2(b) can be applied. In this case, the characteristic impedance and the propagation constant read

$$Z_c = \frac{\omega\mu}{\beta},\ \beta = \omega\sqrt{\mu(\epsilon - j\epsilon')} \tag{13}$$

where Z_c and $\beta = \beta' - j\beta''$ respectively represent the characteristic impedance and complex propagation constant of each medium, i.e., skin or glucose, ϵ and ϵ' are the real and imaginary parts of permittivity, ω is the angular frequency of the incident wave, and μ is the vacuum permeability. Varying the permittivity of the middle medium changes its characteristic impedance, which can be detected by the ATR shift.

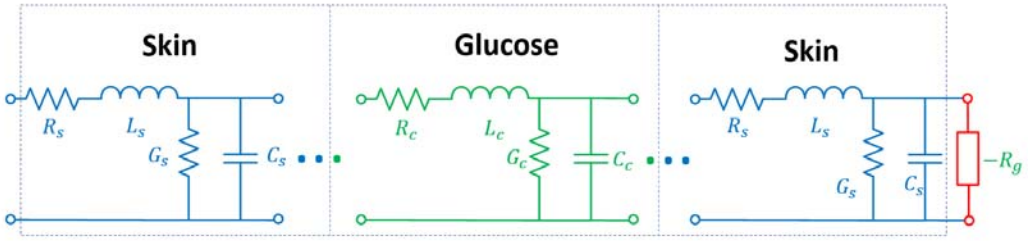

FIG. 5. Discrete-element transmission-line circuit model of the multilayer SGS considering distributed losses.

In practice, the skin and capillary suffer from absorption losses, which should be considered. In our transmission line model, such losses can be incorporated by considering distributed resistance and reactance, as shown in Fig. 5. Clearly, introducing distributed losses alters the original configuration, particularly disrupting the delicate loss and gain balance required for the PT-symmetry conditions. However,

the sensing mechanism based on the shift in ATR persists in this structure, and the ATRs occur at the frequencies where

$$\frac{\partial|Z_e(\omega,\epsilon)-\xi|}{\partial\omega}=0 \tag{14}$$

In this case, we replace the loss element at the input port, and replace it with the distributed losses in the skin layer. The gain element therefore balances the loss in the SGS multilayer. The reflection and transmission coefficients of the modified network are shown in Fig. 6. Here, a negative resistance $R_g = 77\ \Omega$ is used for the active load. The permittivity of skin and glucose are obtained from Ref. [38] and Ref. [10], respectively.

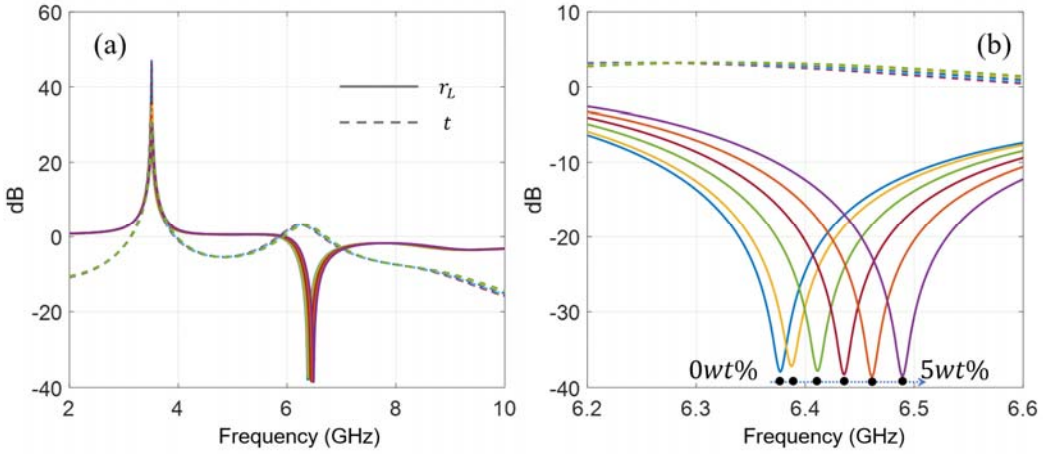

FIG. 6. (a) Transmission and reflection coefficients for different glucose concentrations ($Z_0 = \sqrt{\mu_0/\epsilon_0}$, $l = 2\ mm$, $l_m = 3\ mm$). (b) Zoom-in around the ATR resonance shows the shift with respect to glucose concentration.

Figure 6 shows the ATR resonance features where the reflection coefficient approaches zero. Here the exact PT-symmetry condition is not satisfied, and according to Eq. (8) the transmission coefficient is no longer equal to unity at resonance, but instead is larger than unity (Fig. 6(b)). Another noticeable feature in Fig. 6(a) is a peak in both reflection and transmission outside the frequency range of interest. Although this point marks the onset of undesired self-oscillations, in principle the limited gain bandwidth prohibits the occurrence of oscillations at such far frequency range once we introduce the proper frequency dispersion of the gain element.

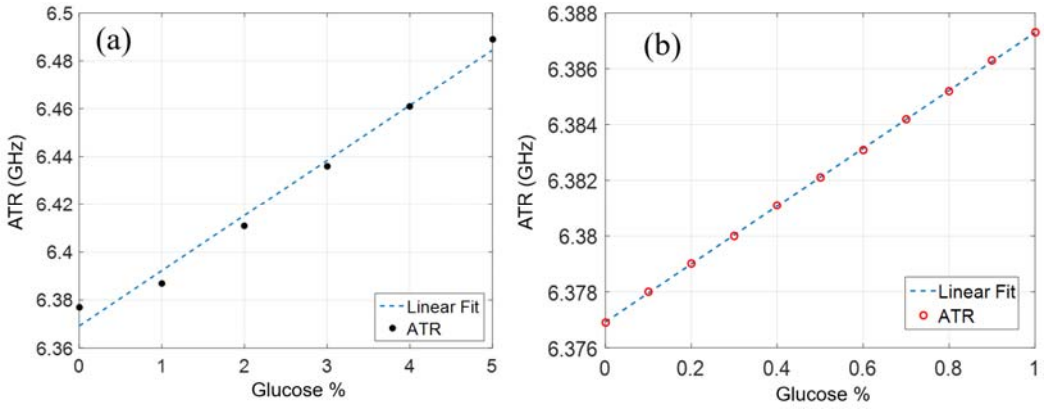

FIG. 7. Piecewise linear trend of the quasi-ATR frequency versus the glucose concentration.

Figure 7(a) shows the variation of the resonance frequency shift with respect to glucose concentration in the range 0wt% to 5wt%. According to this figure, a piecewise linear curve offers a very good fit. In the next section, we analyze and design a realistic 3D sensor based on this concept.

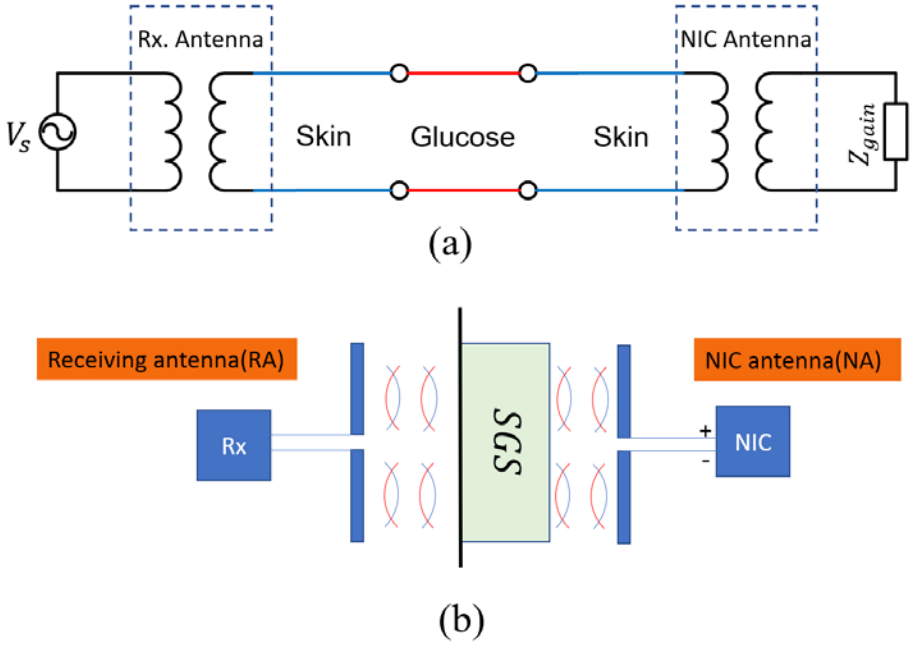

FIG. 8. Realistic implementation of the glucose sensor, including an oscillator and two coupling antennas. (a) Circuit model. (b) Schematic representation of the configuration of interest.

IV. REALISTIC SENSOR DESIGN AND SIMULATION

A realistic configuration for the PT glucose sensor is schematically depicted in Fig. 8,

in which we consider transmitter and receiver antennas on the two sides of the SGS multilayer. On the left side we define a transmitting port, which generates the impinging signal and detects the reflection of the incident wave from the sample. On the right side we define a negative impedance circuit (NIC) coupled to the skin through a coupling antenna. The configuration of this system is shown schematically in Fig. 8(b).

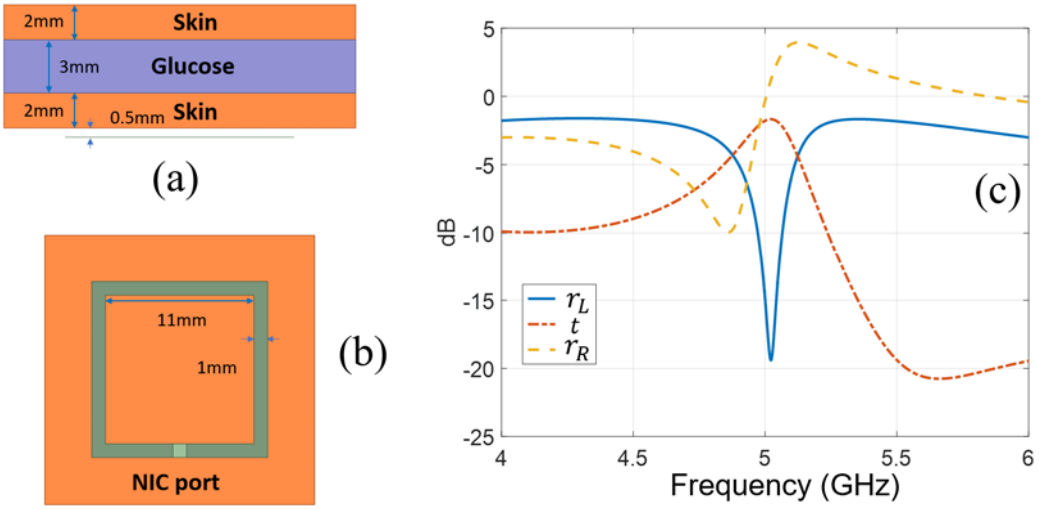

FIG. 9. Full-wave simulation (ANSYS HFSS) of the periodic SGS model through the finite element method. (a) A side view of the SGS multilayer under analysis. (b) A top view of the sample and of the structure, including the coupling loop antenna and the negative impedance circuit. (c) Finite-element simulated results for the reflection and transmission coefficients of the proposed sensor. Here we consider a negative impedance $R_g = -95\ \Omega$.

In order to simulate the operation of the proposed configuration, we first use the finite element method on an infinite SGS multilayer. We use periodic boundary conditions and simulate the structure shown in Figs. 9(a, b) as a unit cell. We perform this simulation because it matches more precisely the analytical model presented in the previous section, which was based on a transversely invariant geometry. As shown in this figure, we utilize a loop coupling antenna between the NIC and skin. Fig. 9(c) shows the simulated results for the scattering coefficients, which reveal a quasi-ATR (associated with 1wt% glucose here). It is noted that, because of coupling at both ends, the ATR frequency and NIC value are slightly modified compared to our analytical model in the previous section. Still, the simulations confirm that the proposed PT-symmetric configuration is a viable approach for high-sensitivity detectors.

We expect deviations between the simulation results based on the infinite periodic structure and those based on an isolated element, given that the SGS is finite and will support fringing fields. Fig. 10(a) shows the results for the individual element, formed by a 3D SGS multi-layer, sandwiched between the same loop antennas considered in Fig. 9, one of which is loaded by the negative impedance load. The structure is relatively easy to tune, correcting for the finite size of the sample, to yield again a quasi-ATR condition, as shown in Fig. 10(c).

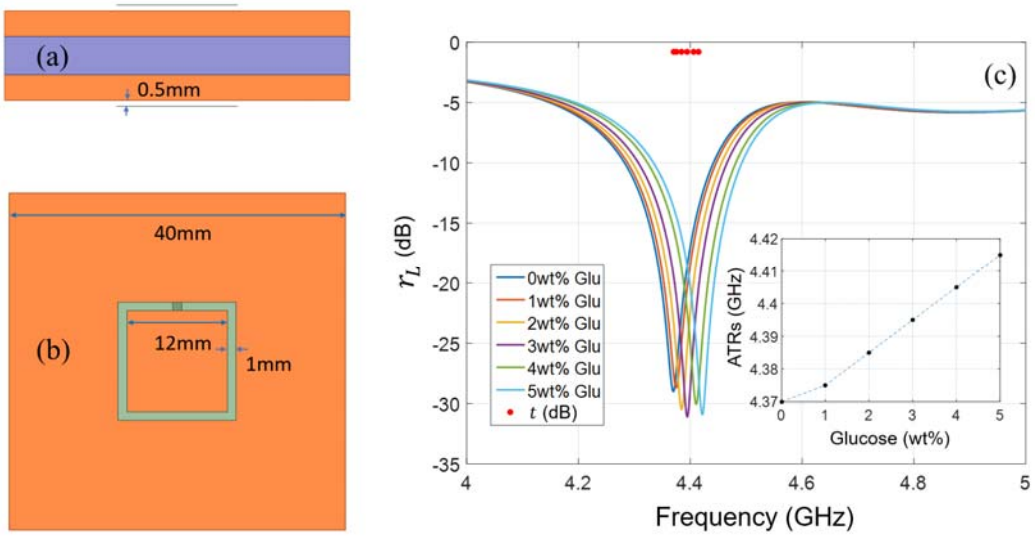

FIG. 10. Finite element simulations of the finite SGS structure. (a) Side view. (b) Top view. (c) Reflection coefficient showing ATRs. The red dots show the transmission coefficient at the ATRs. The inset in part shows the ATR frequency versus the concentration of glucose.

The figure shows the finite-element simulation results for the finite SGS structure. Here, two similar loop antennas are used and the gap between antennas and skin is assumed to be 0.5 mm. Because a single port is employed, the transmission coefficient cannot be evaluated directly. Two cross-sections on both sides of the structure are chosen to calculate the input and output power, which are used to calculate the transmission coefficient as

$$S_{21} = \frac{\iint \overline{E_{in}} \times \overline{H_{in}^*} \cdot d\overline{S_{in}}}{\iint \overline{E_{out}} \times \overline{H_{out}^*} \cdot d\overline{S_{out}}} \quad . \tag{9}$$

In this relation, $\bar{E}$ and $\bar{H}$ represent the time-harmonic electric and magnetic field vectors respectively, ds is a unit of surface integration, and the subscripts “in” and “out” show the input and output cross section planes. The transmission coefficients, calculated at each minimum reflection point, are shown in Fig. 10(c) with red dots. As

these results clearly indicate, each minimum reflection point is a quasi-ATR. It is observed that the ATRs are linearly related with the glucose concentration also in this realistic scenario.

The thickness of skin and glucose layers are not constant when considering different body parts and different persons. In addition, other errors and uncertainties arise from the gap between the loop antennas and skin, as well as the value of the negative impedance. Hence, it is necessary to investigate the sensitivity of the ATR feature with respect to such parameters.

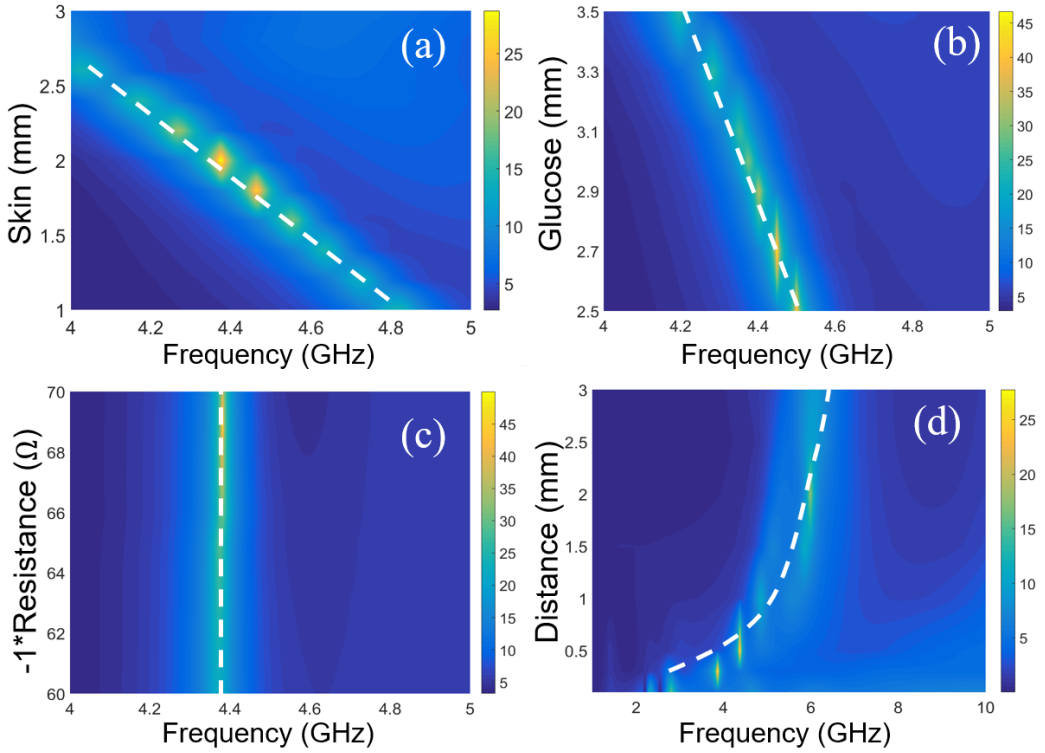

FIG. 11. Sensitivity of ATRs to key parameters including (a) skin thickness, (b) glucose thickness, (c) negative impedance, and (d) gap between the sample and the loop antennas. In all cases, the horizontal axis shows the frequency, and colors depict the magnitude of the reflection coefficient. The dashed line shows the evolution of the resonance feature as parameters change.

Figure 11 shows the reflection spectrum in terms of the variations of the thickness of skin and glucose, negative impedance and distance between loop antenna and skin. According to this figure, the ATR feature is robust in all cases, while the resonance evolves in frequency. In principle, the errors can be simply calibrated for each scenario. As one would expect, Figs. 11(a, b) show that the ATRs change linearly with

the variation of the skin and glucose layers, thus the proposed sensor can be simply adjusted for its use with samples with different thicknesses.

V. NEGATIVE IMPEDANCE CIRCUIT (NIC) AND DISPERSION

As discussed in previous sections, the negative impedance circuit forms an important part of the system in order to realize the PT-symmetry condition and the formation of the ATR feature. In reality, the negative impedance circuit is expected to exhibit frequency dispersion, which we did not consider in the previous results. Equation (14), however, can be still applied to the system after incorporating the dispersion relation into ξ. In addition, the NIC stability, guaranteeing its realizability in experiments, needs to be explored. In this paper, considering the easiness of implementation, the NIC is designed based on operational amplifiers. In particular, we consider the operational amplifier TI THS4303. This device exhibits wideband gain. As discussed in the Appendix, we introduce an external feedback into this operational amplifier in order to achieve the desired negative impedance in the frequency range of interest. The calculated input impedance of the NIC is shown in Fig. 12, clearly showing the negative resistance in the frequency range of interest. As this figure indicates, the negative impedance is highly dispersive.

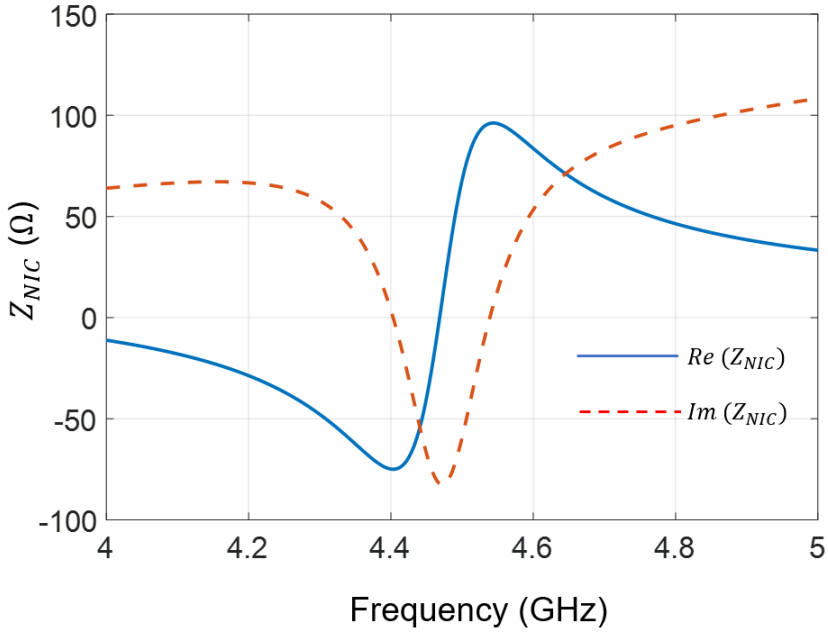

FIG. 12. Input impedance of the NIC element

Figure 13 shows the simulated results considering the dispersive input impedance

calculated in Fig. 12. It is observed that the ATRs are slightly affected by the dispersion, but still follow a nice linear trend with respect to the concentration of glucose, ensuring that a realistic implementation of these concepts is within reach. We have also analyzed the stability of the system and, as discussed in the Appendix, we find that the simple one-pole model of the active circuit ensures inherent stability of the system in its operation.

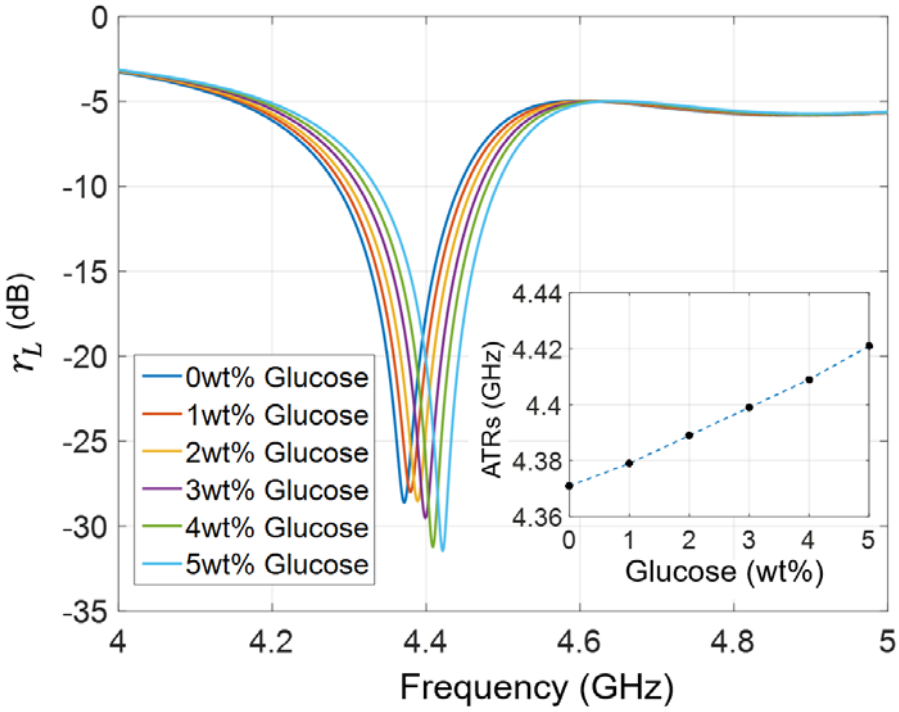

FIG. 13. Simulated reflection coefficients considering the realistic dispersion of the negative impedance circuit.

VI. CONCLUSIONS

In this paper, we have proposed a PT-symmetric configuration for non-invasive detection of glucose. We mapped the skin-capillary-skin geometry of interest to a transmission-line model, and showed that a combination of gain, loss and dispersion can be utilized for sensing purposes. The method establishes the relation between asymmetric transmission resonances and glucose concentration changes, improving the accuracy and applicability of traditional non-invasive glucose detection. A realistic low-cost configuration was proposed for implementing such a sensor, and the device was simulated with finite elements. The sensitivity to errors, including the thickness of skin and capillary, negative impedance and location of antennas were analyzed, showing robustness to reasonable variations of these parameters, and the possibility to

calibrate the system to a specific geometry of interest.

APPENDIX: NEGATIVE IMPEDANCE CIRCUIT

A convenient and low-cost way to realize negative impedance responses is to use off-the-shelf operational amplifiers. A schematic of an NIC is shown in Fig. A1.

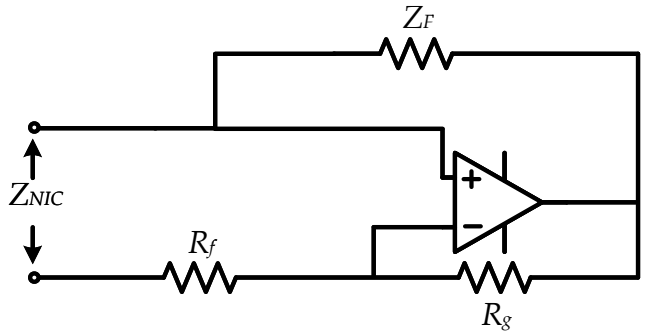

FIG. A1. NIC based on operational amplifier

Consider a low-pass gain for the open-loop amplifier as follows

$$A(s) = \frac{A_0}{1+j\omega/\omega_p} \tag{A1}$$

where, A_0 is the open loop gain at DC, and $f_p = \omega_p/2\pi$ is open loop bandwidth. Then, input impedance, Z_{NIC} can be written as

$$Z_{NIC} = \frac{Z_F}{1-G(j\omega)} = \frac{j\omega+A_0\beta\omega_p}{j\omega+A_0(\beta-1)\omega_p} Z_F \tag{A2}$$

where, G is the gain of closed-loop operational amplifier with the negative feedback factor

$$\beta = \frac{R_f}{R_f+R_g}. \tag{A3}$$

The input impedance can thus be calculated as

$$Z_{NIC} = Z_F \frac{\omega^2+(A_0\omega_p)^2\beta(\beta-1)-j\omega A_0\omega_p}{\omega^2+[A_0\omega_p(\beta-1)]^2} \tag{A4}$$

Assuming that Z_F is a resistance, it is observed that only if $\omega < A_0\omega_p\sqrt{\beta(1-\beta)}$, negative impedance can be realized. THS4303 has a wideband fixed gain, however, the bandwidth of the internal open-loop gain is not enough to provide negative impedance for the range of 4 GHz to 5 GHz. However, the external feedback can be added to achieve that the required negative impedance. In addition, we can lower the gain of the close-loop amplifier to extend the bandwidth ω_p. The topology of the NIC is shown in Fig. A2. L_L and C_L are added to offset the imaginary part of the

negative impedance.

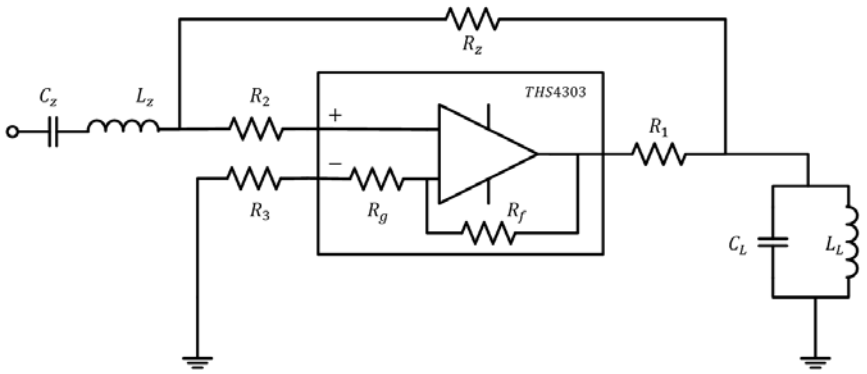

FIG. A2. The circuit topology of NIC using external feedback network.

An LC load is added to ensure the stability. Because the device THS4303 is a multipole amplifier within the required frequency band, the specific function like equation (A1) is not precise to be extracted, the stability is analyzed in time domain as shown in Fig. A3. The input impulse with width of 1.2 ns and magnitude of 1 V is used. We can observe that the NIC without LC load oscillates with an unbounded-output. When LC load is added, the output decays rapidly with a bounded-output, which can be understood that the LC load guarantees that all poles lie within the left-half of s-plane.

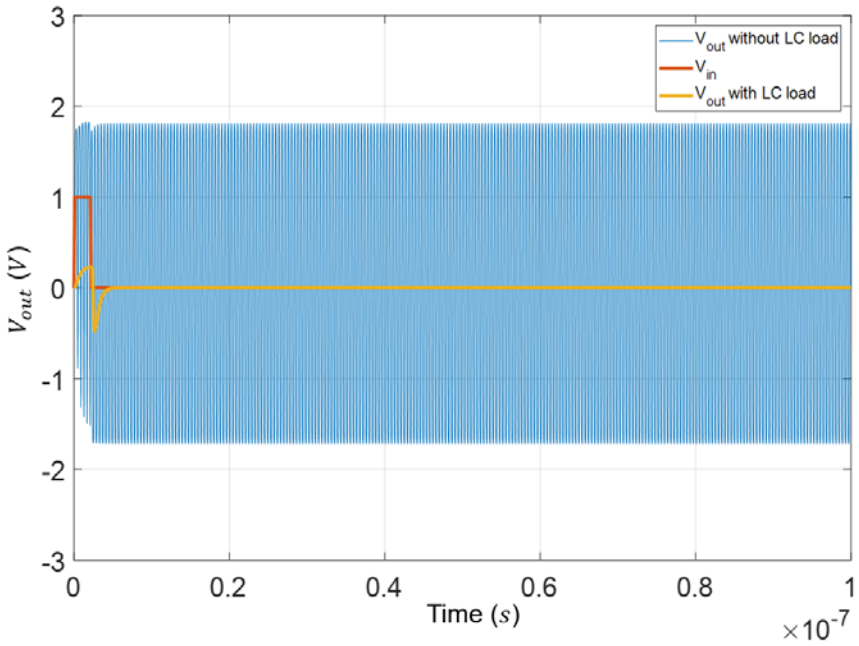

FIG. A3. The response of input impulse with and without LC load.

ACKNOWLEDGMENTS

This work was partially supported by the National Science Foundation, Welch Foundation with grant No. F-1802, Innovate UK Project No. 103862, the China Scholarship Council, and the National Natural Science Foundation of China with Project No. 61671328.

REFERENCES

[1] S. K. Vashist, Non-invasive glucose monitoring technology in diabetes management: A review, Anal. Chim. Acta 750, 16 (2012).

[2] C. E. F. do Amaral and B. Wolf, Current development in non-invasive glucose monitoring, Med. Eng. Phys. 30, 541 (2008).

[3] R. O. Esenaliev, K. V. Larin, I. V. Larina, and M. Motamedi, Noninvasive monitoring of glucose concentration with optical coherent tomography, Opt. Lett. 26, 992 (2001).

[4] C. F. So, K. S. Choi, T. K. Wong, and J. W. Chung, Recent advances in noninvasive glucose monitoring, Med. Devices. 5, 45 (2012).

[5] O. K. Cho, Y. O. Kim, H. Mitsumaki, and K. Kuwa, Non-invasive measurement of

glucose by metabolic heat conformation method, Clin. Chem. 50, 1894 (2004).

[6] T. Glennon, et al., 'SWEATCH': a wearable platform for harvesting and analyzing sweat sodium content, Electroanalysis 28, 1283 (2016).

[7] R. O. Potts, J. A. Tamada, and M. J. Tierney, Glucose monitoring by reverse iontophoresis, Diab. Meta. Res. Rev. 18, S49 (2002).

[8] J. Heikenfeld, Non-invasive analyte access and sensing through eccrine sweat: challenges and outlook circa, Electroanalysis 28, 1242 (2016).

[9] J. Moyer, D. Wilson, I. Finkelshtein, B. Wong, and R. Potts, Correlation between sweat glucose and blood glucose in subjects with diabetes, Diabetes Technol. Ther. 14, 398 (2012).

[10] M. Hofmann, G. Fischer, R. Weigel, and D. Kissinger, Microwave-based noninvasive concentration measurements for biomedical applications, IEEE Trans. Microw. Theo. Tech. 61, 2195(2013).

[11] R. Dobson, R. Wu, and P. Callaghan, Blood glucose monitoring using microwave cavity perturbation, Electron. Lett. 48, 905(2012).

[12] H. Canogarcia, P. Kosmas, I. Sotiriou, I. Papadopouloskelidis, C. Parini, I. Ioannis Gouzouasis, G. Palikaras, and E. Kallos, Detection of glucose variability in saline solutions from transmission and reflection measurements using V-band waveguides, Meas. Sci. Technol. 26, 125701 (2015).

[13] S. Saha, et al, A glucose sensing system based on transmission measurements at millimeter waves using micro strip patch antennas, Sci. Report 6855 (2017).

[14] C. M. Bender and S. Böttcher, Real spectra in non-Hermitian Hamiltonians having PT symmetry, Phys. Rev. Lett. 80, 5243 (1998).

[15] K. G. Makris, R. El-Ganainy, and D. N. Christodoulides, Beam dynamics in PT symmetric optical lattices, Phys. Rev. Lett. 100, 103904 (2008).

[16] R. El-Ganainy, K. G. Makris, M. Khajavikhan, Z. H. Musslimani, S. Rotter, and D. N. Christodoulides, Non-Hermitian physics and PT symmetry, *Nat. Phys.* 14, 11 (2018).

[17] A. Regensburger, C. Bersch, M. A. Miri, G. Onishchukov, D. N. Christodoulides, and U. Peschel, Parity–time synthetic photonic lattices. Nature 488, 167 (2012).

[18] A. Guo, G. J. Salamo, D. Duchesne, R. Morandotti, M. Volatier-Ravat, V. Aimez, G. A. Siviloglou, and D. N. Christodoulides. Observation of PT-symmetry breaking in complex optical potentials, Phys. Rev. Lett. 103, 093902 (2009).

[19] Z. Lin, H. Ramezani, T. Eichelkraut, T. Kottos, H. Cao, and D. N.

Christodoulides, Unidirectional invisibility induced by PT-symmetric periodic structures, Phys. Rev. Lett. 106, 213901 (2011).

[20] R. Fleury, D. L. Sounas, and A. Alù, Negative refraction and planar focusing based on parity-time symmetric Metasurfaces, Phys. Rev. Lett. 113, 023903(2014).

[21] S. Longhi, PT-symmetry laser absorber. Phys. Rev. A 82, 031801(R) (2010).

[22] M.-Ali Miri, P. LiKamWa, and D. N. Christodoulides, Large area single-mode parity–time-symmetric laser amplifiers, Opt. Lett. 37, 764 (2012).

[23] H. Hodaei, M.-Ali Miri, M. Heinrich, D. N. Christodoulides, and M. Khajavikhan, Parity-time-symmetric micro-ring lasers, Science 6212, 346 (2014).

[24] R. Fleury, D. L. Sounas, and A. Alù, An invisible acoustic sensor based on parity-time symmetry, Nat. Commun. 6, 5905 (2015).

[25] Y. Ra'di, D. L. Sounas, A. Alù, and S. A. Tretyakov, Parity-time-symmetry teleportation, Phys. Rev. B 93, 235427 (2016).

[26] S. Assawaworrarit, X. Yu, and S. Fan, Robust wireless power transfer using a nonlinear parity-time symmetric circuit, Nature, 546 (2017).

[27] L. Ge, Y. D. Chong, and A. D. Stone, Conservation relations and anisotropic transmission resonances in one-dimensional PT-symmetry photonic heterostructure, Phys. Rev. A 85, 023802 (2012).

[28] G. Castaldi, S. Savoia, V. Galdi, Andrea Alu, and N. Engheta, PT metamaterials via complex-coordinate transformation optics, Phys. Rev. Lett. 110, 173901 (2013).

[29] C. Shi, M. Dubois, Y. Chen, L. Cheng, H. Ramezani, Y. Wang, and X. Zhang, Accessing the exceptional points of parity-time symmetric acoustics, Nat. Commun. 7, 11110 (2016).

[30] R. Boyd, B. Leigh, and P. Stuart, Capillary versus venous bedside blood glucose estimations, Emerg. Med J. 22, 177 (2005).

[31] P. F. M. Smulders, M. G. Buysse, and M. D. Huang, Dielectric properties of glucose solutions in the 0.5–67 GHz range, Microw. Opt. Technol. Lett. 55, 1916 (2013).

[32] P. Höchtl, S. Boresch, and O. Steinhauser, Dielectric properties of glucose and maltose solutions, J. Chem. Phys. 112, 9810 (2000).

[33] G. W. Yoon, Dielectric properties of glucose in bulk aqueous solutions: influence

of electrode polarization and modelling, Biosens. Bioelectron. 26, 2347 (2011).

[34] P.-Y. Chen, M. Sakhdari, M. Hajizadegan, Q. Cui, M.M.-C. Cheng, R. El-Ganainy, and A. Alu, Generalized parity-time symmetry condition for enhanced sensor telemetry, Nat. Electronics 1, 297 (2018).

[35] P. -Y. Chen and J. Jung, PT symmetry and singularity-enhanced sensing based on photoexcited graphene Metasurfaces, Phys. Rev. Appl. 5, 064018 (2016).

[36] G. Castaldi, S. Savoia, V. Galdi, A. Alu, & N. Engheta, P T metamaterials via complex-coordinate transformation optics, Phys. Rev. Lett. 110, 173901 (2013).

[37] S. Longhi, Invisibility in-symmetric complex crystals, Journal of Physics A: Mathematical and Theoretical, 44(48), 485302(2011).

[38] D. M. Pozar, Microwave Engineering, Hoboken, NJ :Wiley (2012).

[39] S. Gabriel, R. W. Lau, and C. Gabriel, The dielectric properties of biological tissues: III. Parametric models for the dielectric spectrum of tissues, Phys. Med. Biol. 41, 2271(1996).

[40] V. Turgul and I. Kale, Characterization of the complex permittivity of glucose/water solutions for noninvasive RF/Microwave blood glucose sensing, Proc. IEEE Int. Instrum. Meas. Technol. Conf (2016).

[41] A. Brady, C. McCabe, and M. McCann, Fundamentals of medical surgical nursing, John Wiley & Sons (2013).

[42] M. Hofmann, G. Fischer, R. Weigel and D. Kissinger, Microwave-Based Noninvasive Concentration Measurements for Biomedical Applications, IEEE Trans. Microw. Theory Techn. 61, 2195(2013).

[43] S. Costanzo, V. Cioffi and A. Raffo, Analytical model for microwave sensors behavior into biological medium, Proc. IEEE Int. Microw. Antennas, Commu. Elect. Syst. Conf. (2017).

[44] O. Cherkasova, M. Nazarov, and A. Shkurinov, Properties of aqueous solutions in THz frequency range, J. Phys.: Conf. Ser. 793, 012005 (2016).